Front. Earth Sci. 2023, 17(4): 956–969
https://doi.org/10.1007/s11707-023-1092-8

RESEARCH ARTICLE

Dust transport information and paleoclimatic changes revealed by the loess in Ranwu, south-eastern Xizang

Meihui PAN (✉)[1,2], Huimin ZHAO[1,2], Anna YANG[3], Yougui CHEN[1,2], Chenlu LI[1,2]

1 College of Geography and Environment Science, Northwest Normal University, Lanzhou 730070, China
2 Key Laboratory of Resource Environment and Sustainable Development of Oasis, Northwest Normal University, Lanzhou 730070, China
3 CAS Key Laboratory of Mountain Hazards and Surface Process, Institute of Mountain Hazards and Environment, Chinese Academy of Sciences (CAS), Chengdu 610041, China

Abstract The loess accumulation process has great potential to record patterns of atmospheric circulation change, paleoclimate, and paleoenvironmental evolution. South-eastern Xizang is a climatically sensitive region and here, we analyze a loess profile at Ranwu in order to explore the processes and interactions of dust transport and paleoclimate evolution in the region. Based on parametric grain size end-member analysis, optically stimulated luminescence (OSL) dating, and environmental proxies we show that the Ranwu loess profile comprises five end members (EMs). EM1 represents the fine silt fraction transported by high-altitude westerly winds over long distances; EM2 represents the medium silt fraction accumulated by glacier winds; EM3 is the coarse silt fraction transported by local dust storms under the action of strong glacier winds; EM4 represents the very fine sand fraction transported by strong local dust storms, different wind strengths controls the relative proportion of EM3 and EM4 over time. EM5 is the coarse sand fraction formed from the product of strong weathering of gravels. OSL dating shows loess sedimentation at Ranwu started around 11.16 ka. The prevailing climate was generally warm and wet between 11.6 and 4.2 ka, with four cooling events at 10.50, 9.18, 7.85, and 6.37 ka. Extensive paleosol development between 8.2 and 4.2 ka, a change to dry and cold climate conditions was favorable for loess formation after 4.2 ka. The palaeoenvironmental changes and abrupt climate events recorded in the Ranwu loess sequence are consistent with Holocene global environmental changes.

Keywords loess, grain size end member, the optically stimulated luminescencethe, dust transport information, environmental evolution, southeastern Xizang region

Received April 3, 2023; accepted August 31, 2023

E-mail: panmh@nwnu.edu.cn

1 Introduction

Loess-paleosol sequences, widespread in China, are an important paleoenvironmental archive and contain significant paleoclimatic information. The sequences are characterized by their great thickness, complete and continuous deposition, and provide an indispensable terrigenous record archive (An et al., 2014; Li et al., 2020). The study of the loess began to flourish in China in the 1960s (Li et al., 2021), focusing on the Loess Plateau, but more recently the Qinghai-Tibet Plateau has been recognized as an important source area of dust to the Loess Plateau as well as an significant loess archive in its own right (Kapp et al., 2011; Heermance et al., 2013). The more complex depositional and erosion processes, and higher loess deposition rates on the Tibetan Plateau (TP) give the potential for Quaternary climate changes to be reconstructed at higher resolution (Lehmkuhl et al., 2014). However, in comparison with the Loess Plateau, the loess archive of the TP is not well-studied.

A range of proxy indicators have been applied to help interpret the loess sediment record. Grain size is a crucial proxy indicator: grain size composition and distribution characteristics reflect sedimentary processes, sedimentary dynamics, sedimentary environment, and sediment sources in the study area (Song et al., 2016). However, traditional grain size parameters are limited in identifying changes in the sedimentary environment, especially with mixed grain size populations (Wang et al., 2018). Weltje (1997) proposed the end-member analysis method to decompose the grain-level components corresponding to different sediment dynamics based on the grain size characteristics of the sediment. The method provides more accurate identification of sediment dynamics and how they change at each stage of the sedimentation process, and can be applied to marine, lake, and eolian sediments (Zhong et al., 2020; Kong et al., 2021; Xu

et al., 2021). Other proxies used as indicators of change in the loess depositional environment include median grain size, magnetic susceptibility, elemental analysis, and chromaticity. Median grain size (*Md*) and frequency-dependent magnetic susceptibility (x_{fd}) have been used to indicate the strength of winter and summer monsoon, changes in climate (cold, warm, dry, and wet), and degree of soil development (An et al., 1991; Ding et al., 2019; Kong et al., 2020). Rb/Sr has been used as an indicator of chemical weathering under the influence of monsoon climate and of changes in monsoon intensity (Dasch, 1969). In chromaticity, redness (a^*) has been shown as an excellent indicator of temperature, reflecting hydrothermal conditions and weathering intensity during soil formation; high values indicate a combination of hydrothermal conditions, warm and wet climate, and intense chemical weathering (Yang and Ding, 2003; Sun et al., 2011; Wang et al., 2015). Proxies combined with dating methods, have been used in several studies to systematically analyze the chronology, genesis, spatiotemporal variability of the Holocene climate, moisture conditions and the associated driving mechanism, variation of dust activity, the paleo-precipitation history, the winter mid-latitude Westerlies and South Asian monsoons in the south-eastern TP (Zan et al., 2013; Li et al., 2018; Gao et al., 2021; Yang et al., 2022; Cheng et al., 2023a, 2023b, 2023c; Ling et al., 2023). The studies show that most loess in the TP and its margins was formed about 0.8–1.15 Ma, and mainly originates from within the plateau (Fang et al., 2004). The variation of dust activity frequency in the southern TP shows strong cyclicity,which is closely related to the changes of the North-Atlantic Oscillation phase in response to solar irradiance forcing (Cheng et al., 2023a). The Holocene evolution of moisture conditions was mainly controlled by changes in the relative intensities of the Indian summer monsoon and the winter mid-latitude Westerlies (Yang et al., 2022).While there is significant Holocene climate variability between the eastern and western regions of the southern TP, the loess deposits in the western and eastern regions are dominated by different winds (Ling et al., 2023).

South-eastern Xizang is influenced by monsoon and westerly circulation systems and is an important location for understanding climatic and environmental changes on the TP, and loess deposits in the region hold a chronological and sedimentary archive of these changes. Zhang et al. (2015) studied loess at Ranwu, they showed the glacier wind as the transport dynamics, most of the loess originated as locally-derived glacier outwash, but they suggested the loess also contained evidence of regional monsoon-driven climate change. To explore paleoclimatic evolution in the region more fully, we need to better understand the influence of atmospheric circulation changes on loess transport dynamics and how that is reflected in the Ranwu loess profile. Here we use the parametric grain size end-member analysis method, combined with optically stimulated luminescence (OSL) dating and environmental proxies (frequency-dependent magnetic susceptibility, median grain size, chromaticity, and Rb/Sr analysis), to disentangle the transport dynamics and paleoclimate significance of different dust fractions of Ranwu loess. The study offers insights into the mechanisms driving climate changes in south-eastern Tibet and to the wider field of paleoclimatology.

2 Regional setting

The study area is located near Ranwu Lake in the Ranwu region of south-eastern Xizang (Fig. 1). To the north and abutting Ranwu Lake is the Laigu glacier, and annual precipitation at the elevation of the glacier equilibrium line is 1000–3000 mm (Xiong et al., 2021) (Fig. 2). The valley is a typical alpine canyon, with the overall topography higher in the north and lower in the south and dense vegetation along both sides of the valley (Zhao et al., 2019). The climate of south-eastern Xizang is temperate subhumid plateau monsoon and is influenced by both the Indian summer monsoon and westerlies, with

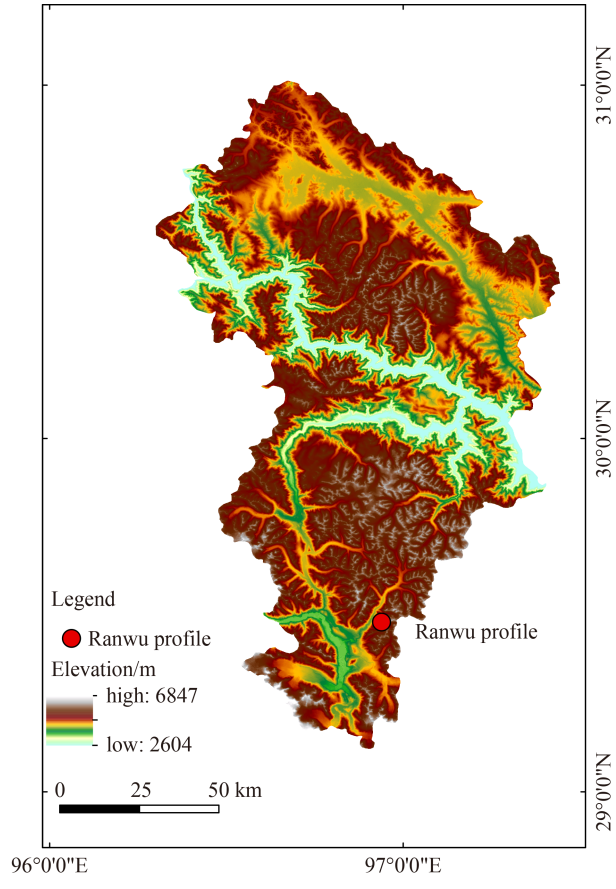

Fig. 1 Location of the Ranwu profile (about 160 cm in depth, 29°26′10.14”N, 96°48′30.06”E).

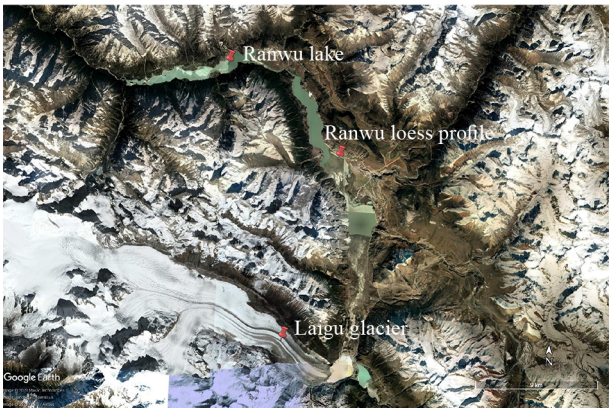

Fig. 2 The depositional environment of the Ranwu loess.

an average annual temperature of about 8.7°C (Zhao et al., 2019). The Indian summer monsoon is dominant in summer, giving wet and cool conditions. Westerly cyclones are dominant in winter, bringing limited moisture, so the climate is cold and dry, with many gusty winds (Thompson et al., 2000). In winter and spring, the Ranwu valley is subject to strong glacier winds from the Laigu glacier that produce local dust storms. The Ranwu loess covers an area of around 1.5 km^2, mainly on river terraces and moraines in the glacial river valleys (Zhang et al., 2015).

3 Methods

3.1 Sample collection

The Ranwu loess profile was sampled at a roadside location next to Ranwu Lake, about 5 km from Ranwu town, at an altitude of 3964 m (Fig. 2). The total thickness of the loess profile at the sampling site is 160 cm. Two continuous samples were collected (RW-1 and RW-2) from the surface downward, and 75 samples were collected at 2 cm intervals from 10 to 160 cm depth (RW-3 to RW-77). Additionally, three luminescence samples were collected for OSL dating at 20, 60, and 140 cm depth (Fig. 3), during the collection, transportation, storage, and pre-processing and testing of optometric dating samples, it is necessary to ensure that the samples are not exposed (except for laboratory red light). In the field, loess and paleosol layers could be clearly distinguished based on differences in color and structure, and after further laboratory observation, six stratigraphic layers were identified (Table A1).

3.2 Laboratory measurements

Sample pre-treatment and grain size testing was undertaken at the Key Laboratory of Resource Environment and Sustainable Development of Oasis, North-west Normal University. Grain size testing was performed using a Malvern Mastersizer 3000 laser grain sizer with a measurement range of 0.02–3500 μm and a repeatable measurement error of less than 2%. The Udden-Wentworth grain size standard was used for grain size classification.

The concentration of elements in 77 samples was measured using a PANalytical Epsilon 4 desktop Energy Dispersive X-ray fluorescence spectrometer from Panaco, the Netherlands. Concentrations of major oxides are given as oxide percentages and trace elements as ppm. Samples need to be air-dried at room temperature before testing, then roots and impurities were removed and they were ground to a grain size of < 200 mesh by vibratory grinding.

Magnetic susceptibility was measured using a Bartington MS2 magnetization meter manufactured in the UK to obtain low-frequency magnetic susceptibility (x_{lf}) and high-frequency magnetic susceptibility (x_{hf}).

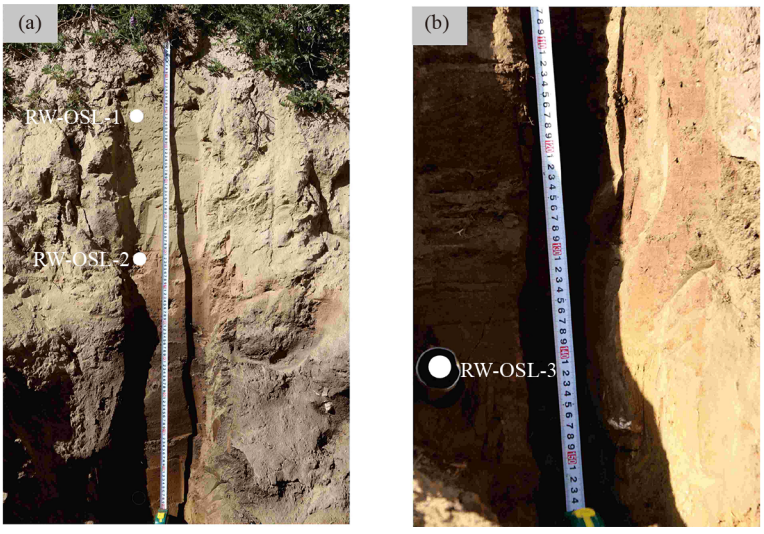

Fig. 3 Field sampling map (a) Sampling profile; (b) White circles denoting the OSL dating sampling site.

Frequency-dependent magnetic susceptibility (x_{fd}) was then calculated using the formula:

$$x_{fd} = \frac{x_{lf} - x_{hf}}{x_{lf}} \times 100\%. \quad (1)$$

A CR-400 color chromatic meter produced by Konica Minolta, Japan, was used for the chrominance test, with a CELAB colorimetric expression system to measure sample brightness (L^*), redness (a^*), and yellowness (b^*).

For OSL dating, 38–63 μm quartz grains were extracted from the OSL samples as test minerals. The equivalent dose (De) determination use a combination of the singlealiquot regenerative-dose (SAR) protocol (Murray and Wintle, 2000) and the standard growth curve (SGC) method (Roberts and Duller, 2004; Lai, 2006). Each sample measured 20 aliquots, using the SAR protocol measured eight aliquots and using SAR to construct SGC, 12 additional aliquots were measured for their natural (LN) and test dose (TN) OSL signal under the same measurement conditions as SAR. The De value was obtained by matching the test dose corrected natural OSL signal in the SGC. For a sample, the final De value was the mean of both the SAR Des and the SGC Des, if the SGC De was within 10% of the SAR De (Liu and Lai, 2012). Pre-processing and computer testing of the luminescence samples was carried out in the Laboratory of Luminescence, Chengdu Institute of Mountain Hazards and Environment, Chinese Academy of Sciences, using a Lexsyg research instrument produced by Freiberg, Germany. The environmental dose rate was calculated by measuring the concentrations of radioactive elements in the surrounding sediments, and the concentrations of U, Th, and K elements in all samples were determined by neutron activation analysis (NAA) and inductively coupled plasma mass spectrometry (ICPMS) at China Institute of Atomic Energy and the Xi'an Geological Survey Center, China, respectively.

3.3 Parametric grain size end-member analysis

Grain size end-member analysis was undertaken to decompose different grain size fractions and their transport dynamics and paleoclimate significance. We used the approach outlined by Paterson and Heslop (2015), who proposed a new parameterized grain size end-member analysis method based on the Weibull function, as it gives improved identification of individual grain size populations in mixed data sets, allowing better indication of deposition dynamics and transport modes of end-member components. The analysis program was run in Matlab and grain size data were imported into the software parametric decomposition. The parametric method is selected by the Gen.Weibull function for analysis (Paterson and Heslop, 2015).

4 Results

4.1 Profile chronology

Figure 4 shows typical OSL decay curves and growth curves for samples RW-OSL-1, RW-OSL-2, RW-OSL-3. The OSL signals decrease very quickly during the first second of stimulation, indicating that the OSL signal is dominated by the fast component. For each sample, the growth curve has not yet reached saturation and can be well fitted using an exponential plus linear function. The test results of OSL samples from the Ranwu loess profile are given in Table 1. Sediments at 20, 60, and 140 cm depth are dated to 0.56 ± 0.13 ka, 2.44 ± 0.17 ka, and 10.00 ± 0.80 ka, respectively, and the three OSL ages are in stratigraphic order. The ages of intermediate strata in the loess profile were determined by linear fitting to the luminescence dates (Fig. 5). The good regression results support deposition of the Ranwu profile between 0 and 11.16 ka, with loess formation before 2.44 ka, paleosol formation between 4.2 and 8.2 ka. Transitional soil formation between 8.2 and 11.16 ka. While previous studies reported the OSL and AMS ^{14}C ages suggest that the Ranwu loess began to accumulate at 6.6 ka and 1.43 ka, the paleosoil was formed at 6.19 ka, the transitional soil was formed at 2.91 ka (Zhang et al., 2015), which may be related to the sampling location of the profile, the sampling depth, the elevation of the profile and the topography.

Based on the OSL dates, fitting ages and the sedimentary characteristics of the profile (Table 1, Fig. 5), the loess profile can be divided into three layers. The bottom layer, 120–160 cm, corresponds to the early Holocene (11.16–8.2 ka) and is composed of transitional soil ($L_{t2}L_{t3}$). The second layer, 72–120 cm, corresponds to the middle Holocene (8.2–4.2 ka) and comprises a paleosol. The third layer, 0–72 cm, corresponds to the late Holocene (4.2 ka to the present) and comprises the transitional soil (L_{t1}), loess, and modern soil.

4.2 Grain size end members analysis

The selection of the number of end members is based on linear correlation, angular deviation, and end-member correlation. To accurately screen the sensitive grain size representing the sediment dynamics of the profile, the number of end members was selected based on achieving higher linear correlation, lower angular deviation (less than 5°), and lower end-member correlation (Bai et al., 2020; Yang et al., 2020; Chen et al., 2021). Comparison of R^2 results for different number of end members (Fig. 6, Table 2) shows that as the number of end members increases, the linear correlation also increases and approaches 1, and the better the grain size curve was fitted to the end members. Nevertheless, the linear correlation drops off again when the number of end

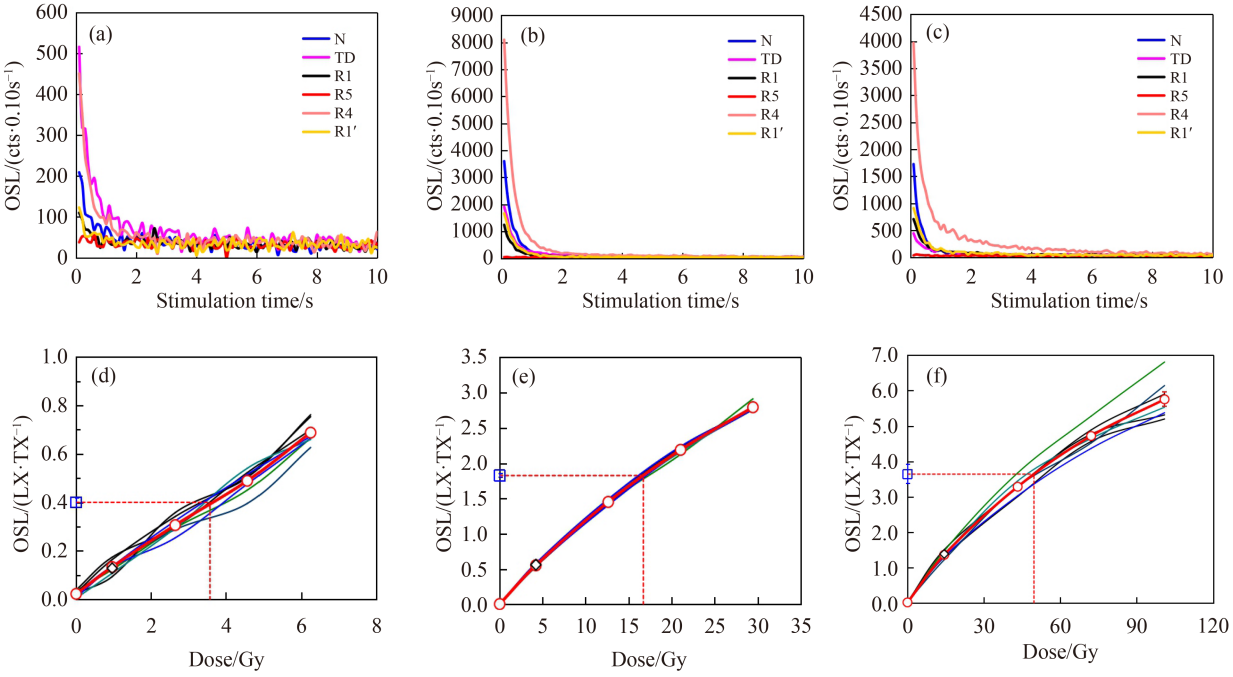

Fig. 4 OSL characteristics of aliquots of samples. (a), (b), (c) Decay curve of OSL signal of RW-OSL-1, RW-OSL-2, RW-OSL-3; (d), (e), (f) Growth curves of the OSL signals obtained using the SAR protocol for RW-OSL-1, RW-OSL-2, RW-OSL-3.

Table 1 Dating results of OSL samples from the Ranwu profile

Depth/cm	U/(μg·g^{-1})	Th/(μg·g^{-1})	K/%	Actual water content/%	Dose rate/(Gy·ka^{-1})	Aliquotnumbers	OSL age/ka
20	3.12 ± 0.4	29.35 ± 0.8	3.15 ± 0.04	8 ± 5	6.29 ± 0.44	8[a)] + 12[b)]	0.56 ± 0.13
60	4.05 ± 0.4	34.39 ± 0.8	3.09 ± 0.04	8 ± 5	6.84 ± 0.48	8[a)] + 12[b)]	2.44 ± 0.17
140	3.53 ± 0.4	21.93 ± 0.8	2.36 ± 0.04	8 ± 5	5.05 ± 0.36	8[a)] + 12[b)]	10.00 ± 0.80

Notes: a) Aliquot numbers using SAR protocol; b) Aliquot numbers using SGC protocol.

members is above 7. When the number of end members is below 3, the angular deviation is greater than 5°, indicting the sensitive grain size representing the depositional dynamics of the profile cannot be accurately screened. When the number of end members is 4, 5, and 6, the angular deviation is 3.28°, 3.16°, and 1.75°, respectively, indicating that angular deviation decreases and fit improves as the number of end members increases. The sensitive grain size representing the sedimentation dynamics of the profile can be accurately screened out when the number of end members is 4, 5, and 6. End-member correlation is 0.7 when the number of end members is 4, 0.12 when the number of end members is 5, and 0.17 when the number of end members is 6. Thus, end-member correlation is lowest when the number of end members is 5; which satisfies the principles of end-member selection and under the condition of satisfying the goodness of fit. Five end members were selected for subsequent data analysis. In addition, van Hateren et al. (2018) suggested that the "geologically feasible" number of end members determined by the algorithms does not necessarily correspond to the true number of end members in a data set. However, the true number of end

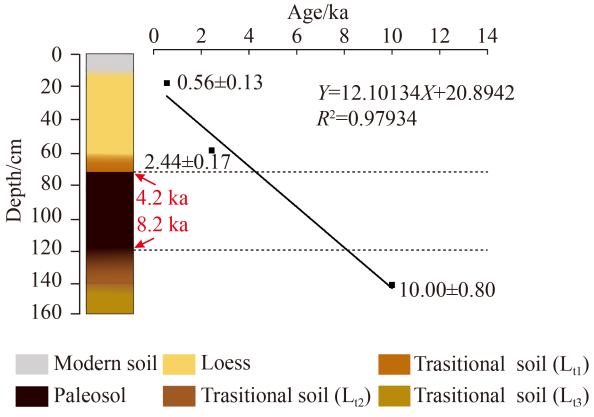

Fig. 5 Age-depth relationship of the Ranwu loess profile.

members is better revealed using class-wise R^2 curves. So, we analyzed the class-wise R^2 of the end-member models with varying numbers of end-members (2–5), results show that when the number of end members is 5, the fitting of each grain size class is the best (Fig. B1).

The end-member characteristics are given in Fig. 6 and Table 2 and summarized below. EM1 mode grain size is

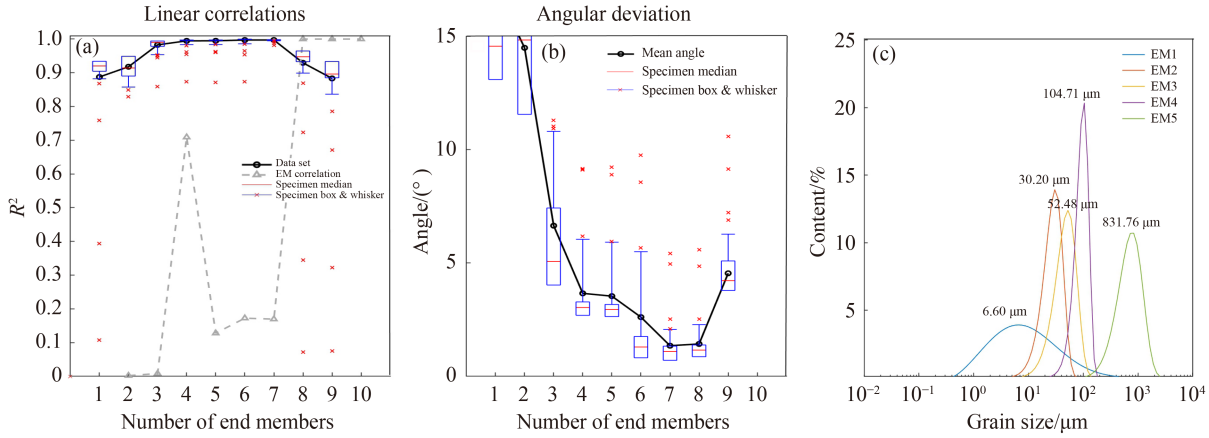

Fig. 6 Results of end member analysis of Ranwu loess profile: (a) linear correlation coefficient; (b) angular deviation; (c) frequency distribution curve of end member.

Table 2 Grain size feature of each end member

Endmember	Mean grain size/(Mz·μm^{-1})	Sorting coefficient	Skewness (Sk)	Kurtosis/kg	Clay particle/%	Silt/%	Sand/%	Gravel/%
EM1	7.72	3.91	0.08	0.96	32.44	60.15	7.41	0
EM2	25.18	1.52	−0.16	1.02	0.06	99.78	0.16	0
EM3	42.73	1.59	−0.15	1.02	0.01	79.68	20.31	0
EM4	85.65	1.34	−0.18	1.06	0	15.39	84.61	0
EM5	641.95	1.68	−0.12	1	0	0	99.64	0.35

6.60 μm, which is a very fine silt. The fraction has high silt content, and is the only end-member fraction containing high clay particle content. This component has the flattest grain size distribution and the worst sorting, reflecting the wider range of grain sizes. EM2 has a mode grain size of 30.20 μm and is a medium silt fraction, with 99.78% silt content, little clay and sand, and better sorting than EM1. The grain size distribution for EM2 has a higher peak and a narrower range. EM3 has a mode grain size of 52.48 μm and is mainly a coarse chalky silt fraction, with higher sand content than EM1 and EM2. EM3 has similar peak area and sorting coefficients as EM2. EM4 has a mode grain size of 104.71 μm, which is a very fine sand fraction, and also contains some chalky silt. The grain size distribution for EM4 has the narrowest peak area, the highest peak value, the smallest sorting coefficient, and the best sorting overall. The mode grain size of EM5 is 831.76 μm, which is mainly a coarse sand component, with a small amount of gravel. EM5 has poorer sorting than EM2, EM3, and EM4, but better than EM1.

4.3 Sedimentary environment

Comparison of the sample grain size frequency distribution curves with those of published grain size distribution curves of loess profiles be used to indicate the sedimentary process environment; curves with similar morphology and peak/mode grain size are judged to have been deposited in the same way (An et al., 2012). In Fig. 7, frequency distribution curves for the loess layer, paleosol layer, and transitional soil layer of the Ranwu profile are compared with those typical of loess from the Loess Plateau (Sun et al., 2004) and from elsewhere in the study region compiled by Zhang et al. (2015). The similar curve morphology of all samples supports a wind-blown origin for sediments in the Ranwu study profile. In addition, the Ranwu profile lacks bedding structures typical of fluvial deposits, such as parallel laminae, interlamination, horizontal laminae, and scouring

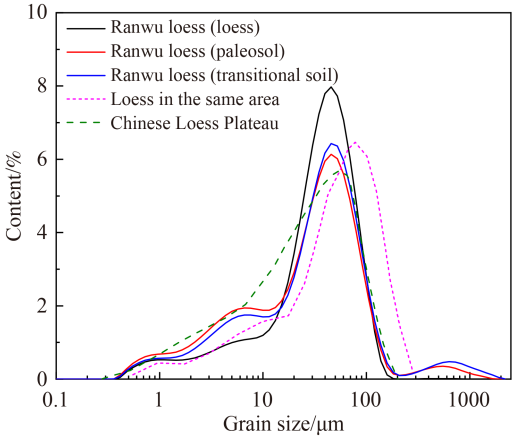

Fig. 7 Grain size distribution curves of Ranwu loess profile (the grain size distribution curves of Ranwu loess, paleosol and transitional soil were compared with the loess in the same region and the Loess Plateau of China).

surfaces, and there is no evidence of rhythmic deposition (Fig. 3), which further supports a wind-blown origin.

4.4 Frequency-dependent magnetic susceptibility, redness, and Rb/Sr

Figure 8 shows the frequency-dependent magnetic susceptibility (x_{fd}), redness (a^*), and Rb/Sr ranges for Ranwu sediments in the early, middle, and late Holocene. Frequency-dependent magnetic susceptibility increases from early to middle Holocene, then decreases from middle to late Holocene. The negative minimum value in the late Holocene may be related to measurement error, or may be a reflection of limited generation of superparamagnetic and magnetic minerals in the soil formation process. The latter would indicate a dry and cold late Holocene depositional environment at Ranwu, with accumulation of less fine-grained material and more coarse-grained material. In addition, there is a significant positive correlation between EM1 and frequency-dependent magnetic susceptibility (Fig. 9), supporting that the fine silt content of the sediments significantly affects the frequency susceptibility value. However, in the early Holocene both the mean and minimum values of frequency-dependent magnetic susceptibility were negative; this is possible due to the high carbonate content of the early Holocene deposits, which reduces the concentration of ferromagnetic minerals and gives a negative susceptibility reading (Fig. B2) (Peck et al., 1994; Xu et al., 2010).

Redness (a^*) and Rb/Sr show similar trends of increasing slightly from early to middle Holocene, then decreasing from middle to late Holocene, with maximum values in the middle Holocene. Correlation analysis of the proxies and end members shows a weak positive correlation between a^* and Rb/Sr and EM1, and a significant negative correlation between a^* and EM2. The results indicate sediment with a higher fine silt content has higher a^* and Rb/Sr, and sediment with higher coarse silt contet is associated with lower a^*. In addition, the range of Rb/Sr is 0.8–2.5, which is consistent with previous study, while the range of a^* is 4–8, it is higher than that of previous study (0.28–0.32) (Zhang et al., 2015), which may be caused by different sampling locations and deposition times of the profile, but the specific reasons need to be further studied in detail.

5 Discussion

5.1 Dust behavior

The parametric grain size end-member analysis of the Ranwu loess profile showed EM1 to have a mode grain size of 6.60 μm, representing a very fine silt fraction. Previous loess studies have suggested that the very fine silt fraction (2 to 16 μm) is susceptible to being lifted to the upper troposphere and transported in suspension over long distances by high-altitude airflow (Vandenberghe, 2013; Yang et al., 2016). Studies of grain size end-

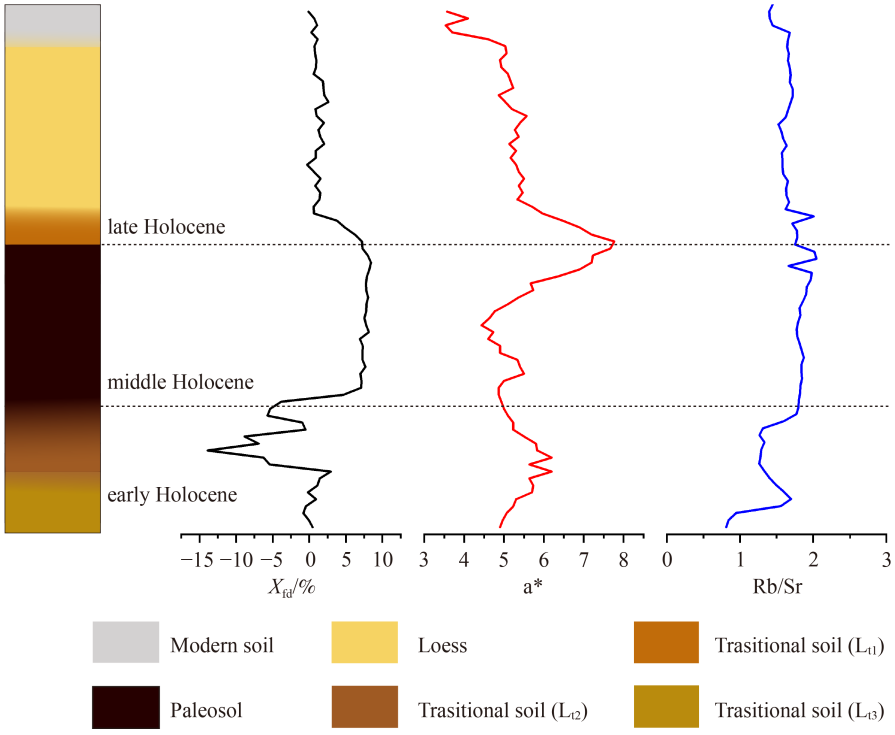

Fig. 8 Changes in x_{fd}, a^*, and Rb/Sr in the Holocene.

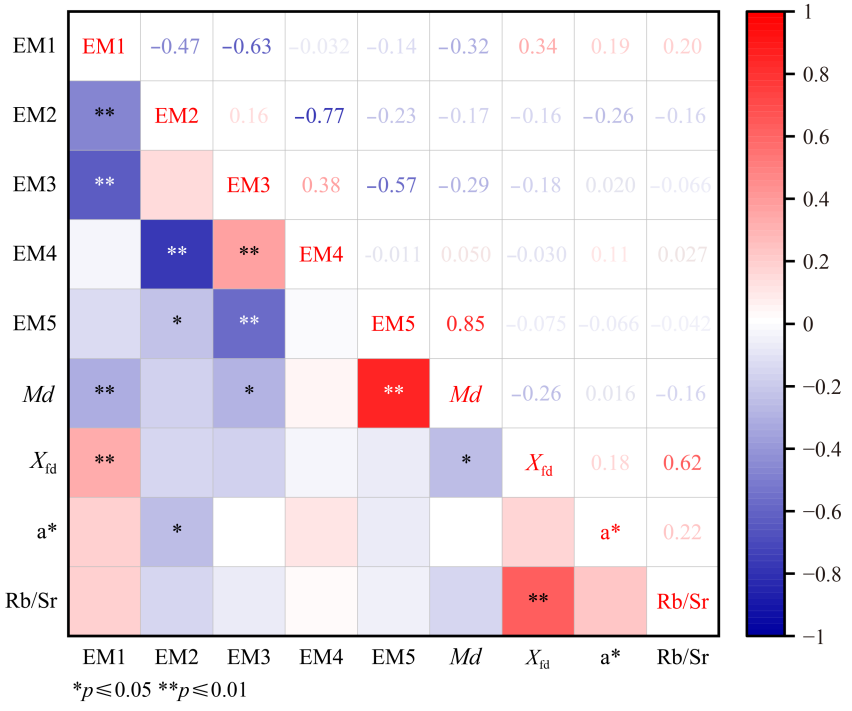

Fig. 9 The correlation between each end member and *Md*, x_{fd}, *a**, Rb/Sr.

member decomposition analysis of loess have indicated high-altitude westerly wind as the transporting agent of the 20 μm fraction (Rea et al., 1985; Sun et al., 2004; Cheng et al., 2018; Chai et al., 2021; Kong et al., 2021). Therefore, Ranwu EM1 is likely to represent the dusty material transported by high-altitude westerly wind. It is worth noting that the fine-grained sediment component, especially the ultrafine component (less than 1 μm), is positively correlated with weathering intensity and soil formation (Sun et al., 2018; Zan et al., 2020) and this may complicate a straightforward dust behavior interpretation. However, only a very small proportion of EM1 sediment in this study is below 1 μm, indicating limited soil-formation processes (Fig. 6(c)). Also, the EM1 fraction is negatively correlated with the other fractions (Fig. 9), indicating it was subject to different transport dynamics and medium than the other fractions.

The mode grain size of EM2 is 30.20 μm; loess grain size fractions ranging from 20 to 70 μm are primarily considered to be transported through low-altitude short-distance suspension in air (Pye, 1987; Sun et al., 2004; Vandenberghe, 2013; Yang et al., 2016; Kong et al., 2021). The higher EM2 peak and narrower range further support the component as representing near-source accumulation. Studies on other loess profiles in the region suggest this grain size fraction is mainly the product of transport by glacier winds and ice-water deposits transported by the winter monsoon (Zhang et al., 2015). Wang and Pan (1997) and Prins et al. (2007) suggested that a similar grain size fraction might be transported by the winter monsoon of the plateau. However, *Md* can respond sensitively to the change of East Asian winter monsoon (Yang and Ding, 2014), there was no significant correlation between EM2 and *Md* indicates that the winter monsoon is not the transporting force of the EM2 fraction at Ranwu (Fig. 9). Hence, we consider glacier wind is the primary transport dynamics of the EM2 fraction, and ice and water accumulation might be the main material source. The high negative correlation between EM2 and EM4 and EM5 may be indicative of different dust source area and transport dynamics.

EM3 is primarily composed of coarse chalky silt particles, with a narrower peak area, indicating near-source accumulation. The mode grain size is below 70 μm, but larger than that of EM2, Nottebaum et al. (2015), Ding et al. (2002) and Pye (1987) suggested that the grain size is coarse, the required transport dynamics is strong and the handling distance is relatively close, so the EM3 fraction has stronger transport dynamics and has a closer source area. And the low correlation between EM2 and EM3 also indicates the two have different transport dynamics (Fig. 9). Chai et al. (2021) suggested the coarse silt grain size fraction represents the dust storm process, and the EM3 mode grain size is very close to that of the Loess Plateau dust storm fraction (55.3 μm), so we infer a dust storm origin for EM3. Dust storms are frequent in the Qinghai-Tibet Plateau in winter and spring, and the highest dust storm occurrence is centered on south-eastern Xizang (Gou et al., 2012). In the Ranwu region, deposition of EM3 is likely associated with the cold and dry winter and spring of the Ranwu valley when strong glacier winds from the Laigu glacier melt sediments on the outwash flood plain and generate local dust storms (Zhang et al., 2015). Hence, we consider EM3 represents

dust material suspended and transported for a short distance by local dust storms under the action of strong glacier winds.

The mode grain size of EM4 (104.71 μm) is in the very fine sand fraction. With the narrowest and highest grain size peak, EM4 is considered to represent coarse-grained sediment that is closest to the source area. The best sorting coefficient reflects the stronger depositional dynamics conditions, with particles sorted several times, and better rounding. The high positive correlation between EM3 and EM4 indicates a similar transport mode (Fig. 9), perhaps with different wind strengths responsible for the differences in grain size sorting, different wind strengths controls the relative proportion of EM3 and EM4 over time (Bokhorst et al., 2011). Hence, we postulate that local dust storms are responsible for the transport and deposition of the EM4 fraction, as for EM3, but the EM4 has stronger transport dynamics. Studies have shown that similar grain size fractions are the major components of dusty sediments in river terraces, such as in the Yellow River, China, and in loess sediments that accumulate near river terraces of the Mississippi River in the United States (Bokhorst et al., 2011; Jacobs et al., 2011), and are considered to be river sediments transported by wind action (Kong et al., 2021; Zhang et al., 2015; Chai et al., 2021). The Ranwu profile sampling site is on a river terrace, so there is potential for the sand-granular fraction of Ranwu sediments to be river-derived. Therefore, we consider EM4 likely represents accumulation of transported fluvial sediments under the action of strong dust storms.

The mode grain size of EM5 is in the coarse sand fraction (831.76 μm), and the range of sizes in the coarse sand range are taken as indicative of variable regional wind and sand activity. This fraction is generally contributed by local sources, such as alluvial and weathered sediments, transported by near-surface winds as creep and saltation load (Long et al., 2007; Li et al., 2018). In the Kumtag Desert, China, it has been suggested that coarse-grained sediments in the 309.52 to 2711.36 μm range originated as the products of intense weathering fragmentation of nearby gravels as it is difficult for this fraction to be transported by wind over long distances (Liang et al., 2020). Therefore, we consider the EM5 component is likely indicative of strong regional variation in wind and sand activity and was sourced from products of intense weathering of gravels. EM5 is highly positively correlated with *Md*, indicating that the coarse-grained component of the Ranwu profile is sensitive to variations in winter monsoon intensity (Kong et al., 2021). Higher EM5 content indicates larger *Md* and higher winter monsoon intensity, indicating the change of EM5 component content is a good indicator for the change of winter monsoon intensity. A high negative correlation between EM5 and EM3 suggests they originate under different processes; EM3 is formed under the action of dust storms, which is presumed to have a small effect on the EM5 component.

The Ranwu loess profile is dominated by EM1 and EM3 components, and they represent the primary dust materials (Table 3). Dust material transportation is mainly driven by westerly winds and local dust storms under the action of strong glacier winds. The lower abundance of EM2, EM4, and EM5 may be attributed to the fine-grained nature of ice-water deposits (source of EM2) and the obstructing effect of strong glacier winds (Ding et al., 2019), which are not conducive to accumulation. Low frequency of strong dust storms and relatively weak weathering may also contribute to lower content of EM4 and EM5 in the profile.

5.2 Paleoclimate evolution of the Ranwu loess profile

The depositing process of the sediments in Ranwu loess profile is a complex process which is influenced by various transport dynamics, pedogenesis and weathering. The comprehensive paleoclimate evolution information of Ranwu loess profile cannot be obtained only through the change of end-member content. Therefore, this paper analyzes the paleoclimate evolution during the accumulation of Ranwu profile through the change of end-member content and environmental proxies (x_{fd}, *Md*, *a**, and Rb/Sr). Figure 10 compares stratigraphic age, sedimentary characteristics, and proxies with the percentages of each parameterized end-member in the Ranwu loess profile in three stages, the early, middle, and late Holocene.

In the early Holocene (11.16–8.2 ka), percentages of all end members fluctuates, with EM1 generally above-average, and EM2 and EM3 generally below average. As ice age glaciers receded, the glacier wind and winter monsoon weakened, dust storm frequency decreased, and climate changed from cold and dry to warm and humid. A thick transitional soil layer ($L_{t2}L_{t3}$) is formed at this stage. At 9.18 ka (134–132 cm) and 10.50 ka (148–146 cm) there are marked fluctuations in each end member and other environmental proxies; at each period, EM3 and EM4 first decrease, then increase, and finally stabilize, while the proxies x_{fd}, *a**, and Rb/Sr all increase and then decrease. These trends indicate that each episode was characterized by strengthening then weakening Indian summer monsoon, warming then cooling climate, and increased then decreased degree of pedogenesis and chemical weathering; suggesting the two episodes comprise abrupt cold and dry weather events. In addition,

Table 3 Contents of different telomeres in the early, middle and late Holocene

	EM1	EM2	EM3	EM4	EM5
Late Holocene	23.91	16.16	53.55	6.28	0.11
Middle Holocene	43.17	8.39	39.48	5.98	2.98
Early Holocene	37.45	8.13	42.74	7.23	4.44

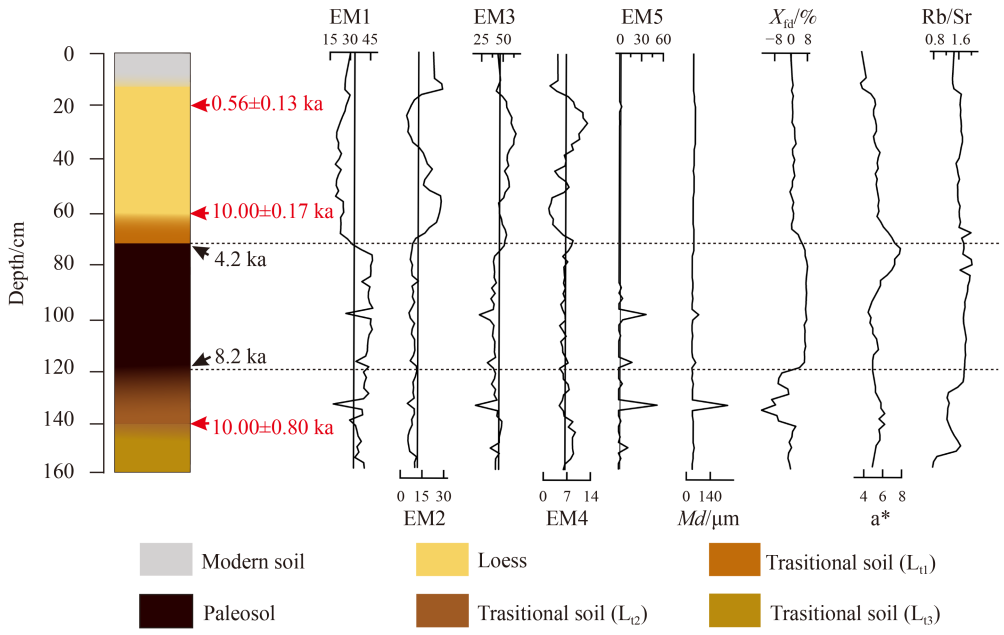

Fig. 10 Comparison of the content of each end member component, x_{fd}, *Md*, *a**, and Rb/Sr in the Ranwu loess profile.

a large number of EM5 components are formed during cold and dry weather events. This could be the result of abrupt climate change. Before the cooling, the gravel mainly suffers from chemical weathering under certain conditions such as temperature and precipitation. During the cooling stage, strong winter monsoon brings strong sand activities, and physical weathering is strengthened. Therefore, the water in the gravel alternates between freezing and thawing, and the rock is prone to collapse and fragmentation, and eventually forming a large number of EM5 components. The two cooling events at Ranwu corresponded to the peat-recorded cooling event (9.1 ka) in the Yangbajing Basin, China, and the North Atlantic ice drift debris event (10.2 ka) (Sun et al., 2016; Wang et al., 2020).

In the middle Holocene (8.2–4.2 ka), *Md* fluctuates a little, and x_{fd} and Rb/Sr levels are higher, indicating a general trend of increasing Indian summer monsoon and weakening winter monsoon, with a warm and humid climate and increased soil development, which is favorable to paleosol formation. At 6.37 ka (98 cm) and 7.85 ka (116 cm), there are clear fluctuations in each end-member: EM1, EM2, and EM3 percentages decrease and then increase. The end-member trends indicating that the strength of westerly circulation, glacier winds, and dust storms first weaken and then increase, the climate first warms and then cools. However, *a** decreases and then increases at each event, indicating weakening followed by strengthening of the Indian summer monsoon. The climate change indicated by *a** is contrary to the climate change indicated by other environmental proxies, which may be due to the different sensitivity of the environmental proxies to climate change, resulting in different indicated climate change. Furthermore, most environmental proxies indicate a cooling climate, and the formation of a large amount of EM5 also indicates a cooling climate. Overall, this points to a change in climate from warm and wet to cold and dry at around 7.85 ka and around 6.37 ka (98 cm). These two climate events correspond to the weak monsoon-generated drought event around 6.5 ka detected by pollen records in Tibetan lake sediments and the 7.9 ka cooling event in the Republican Basin, China peat record, respectively (Shen, 2003; Wang et al., 2002). Zhang et al. (2015) also suggest that there was a drought stage in Ranwu at about 6.66−6 ka, which correspond to the cooling event studied in this paper.

In the late Holocene (4.2–0 ka), the proxies x_{fd}, *a**, and Rb/Sr fluctuate reduction, indicating weakened Indian summer monsoon and strengthened winter monsoon. A change in climate from warm and wet to cold and dry weakened soil formation and the chemical weathering, chemical weathering is weakened, favoring loess accumulation. Based on variations in the end members, two transition points are evident, at 20 and 60 cm, delimiting different climate stages. At 4.20–2.44 ka (72–60 cm), EM1, EM3, and EM4 content decreases and EM2 content increases, reflecting weakened westerly circulation, strengthened glacier winds, and reduced frequency of dust storms. As the climate transitions from warm and wet to cold and dry, *a** decreases significantly, soil development is weakened and a transitional paleosol layer is formed. At 2.44–0.56 ka (60–20 cm), *a** continues to decrease slowly, and the climate is cold and dry, encouraging formation of a loess layer. In the surface section (20–0 cm), the percentages of EM1 and EM2 first increase then decrease, with EM4 following an inverse trend of decreasing then increasing, indicating the westerly and glacier winds first increase and then decrease. The frequency of strong dust storms also

decreases, and the depositional profile transitions from cold and dry to warm and wet. The content of EM5 is close to 0, indicating that although the winter monsoon in the late Holocene were enhanced, the near-surface winds were dominated by glacier winds and local sandstorms, and the winter monsoon had to reach a certain strength to form EM5. In addition, it can be seen from Fig. 4 that there is considerably greater thickness of dust accumulation in this stage than in the early and middle Holocene. The main factors influencing dust material accumulation are the supply from dust source areas, the strength of dust transport distance and transport dynamics, and the ability of the surface to capture dust (Rea et al., 1985; Sweeney and Mason, 2013; Újvári et al., 2016). It is likely that during the climate transition from warm and wet to cold and dry in the late Holocene, stronger glacier wind transport dynamics and closer and more abundant material sources, combined with dense valley vegetation that increased the ability of surfaces to capture dust, were the primary drivers of the thicker accumulation.

6 Conclusions

Parametric grain size end-member analysis was used to decompose the end-member components of sediments in the Ranwu loess profile, south-eastern Xizang, to investigate transport dynamics and transport mode of the sediments in the region. OSL dating was combined with environmental proxies, including frequency-dependent magnetic susceptibility, median grain size, chromaticity, and Rb/Sr, to analyze the paleoenvironmental record of Ranwu. The key conclusions are outlined below.

1) The Ranwu loess profile began to accumulate around 11.16 ka and continues through to the present day, indicating the sediment archive holds a record of from the early Holocene (11.16 ka), during which it experienced a series of cold and warm climate changes.

2) The Ranwu loess profile can be divided into five end members based on grain size fractions. EM1 is the fine silt fraction transported by high westerly winds over long distances; EM2 is the medium silt fraction accumulated by glacier winds; EM3 is the coarse silts fraction transported and accumulated in local dust storms; EM4 is the very fine sand fraction transported by strong dust storms; EM5 is the coarse sand fraction formed from the product of strong weathering of gravels, and is a good proxy of winter monsoon intensity and climate fluctuations over the Holocene. The EM1 and EM3 fractions are the most abundant in the profile and comprise the main dust materials in Ranwu loess. Dust storms generated by westerly winds and strong glacier winds are the main driving force of dust material transport in the Ranwu loess profile.

3) Based on analysis of changes in end members and proxies, the climatic evolution of the Ranwu region in the south-eastern Tibet is reconstructed. In the early Holocene (11.16–8.2 ka), winter monsoon and glacier wind weakened, the Indian summer monsoon strengthened. the climate was warm and wet, and cooling events occurred at 10.50 and 9.18 ka. In the middle Holocene (8.2–4.2 ka), the Indian summer monsoon continues to strengthened, the winter monsoon weakened, the climate was warm and wet, and cooling events occurred at 7.85 and 6.37 ka. In the late Holocene (4.2–0 ka), glacier winds strengthened, local dust storms intensified, and the climate changed from warm and wet to dry and cold, which was favorable to loess formation. The four abrupt climate change events and other paleoenvironemtnal changes recorded in the Ranwu profile are consistent with Holocene global environmental changes.

4) The thickness of sediment accumulation in the late Holocene transition from warm and wet to cold and dry is greater than that of the early and middle Holocene. This is due to stronger glacier wind transport dynamics, closer and more abundant dust sources, and the sediment trapping of dense valley vegetation in the late Holocene.

Acknowledgments This research was supported by the National Natural Science Foundation of China (Grant No. 41807448).

Competing interests The authors declare that they have no competing interests.

Appendice

Table A1 Stratigraphic description of the Ranwu loess profile

Profile layering	Sample depth/cm	Color	Profile description
1	0–10	Off-white	Modern soil, silty sand, modern root development
2	10–60	Light tawny	Loess layer, massive, silty, no structure, relatively loose
3	60–72	Brownish red	transitional soil, massive, clay silt, with roots, developing calcareous mycelium
4	72–120	Black	paleosol layer, clumps, clay silt, root development, calcareous mycelium development
5	126–140	Dark Brown Red	transitional soil, blocky, slightly more colored than the upper layer Shallow, clay silty sand, relatively compact
6	140–160	Tawny	transitional soil, powdery fine sand, harder

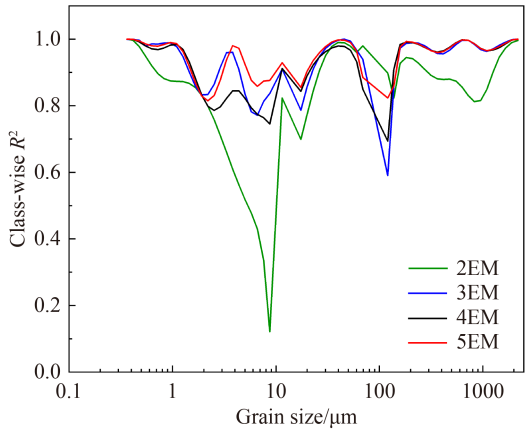

Fig. B1 Class-wise R^2 of the end-member models with varying numbers of end-members.

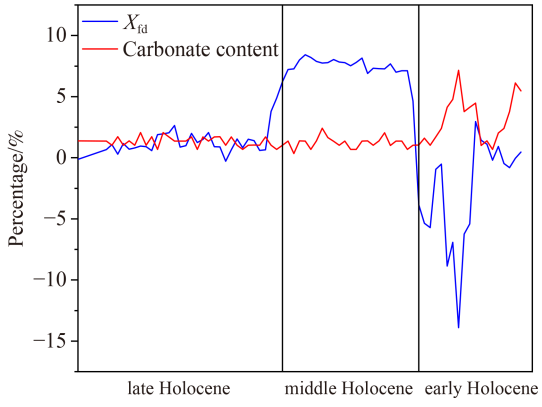

Fig. B2 Variation of frequency-dependent magnetic susceptibility and carbonate content in Ranwu profile in Holocene.

References

An F Y, Ma H Z, Wei H C, Lai Z P (2012). Distinguishing aeolian signature from lacustrine sediments of the Qaidam Basin in northeastern Qinghai-Tibetan Plateau and its palaeoclimatic implications. Aeolian Res, 4: 17–30

An Z S, Kukla G, Porter S C, Xiao J L (1991). Late Quaternary dust flow on the Chinese Loess Plateau. Catena, 18(2): 125–132

An Z S, Sun Y B, Zhou W J, Liu W G, Qiang X K, Wang X L, Xian F, Cheng P, Burr G S (2014). Chinese loess and the East Asian Monsoon. In: An Z, ed. Late Cenozoic Climate Change in Asia. Springer: 23–143

Bai M, Lu R J, Ding Z Y, Wang L D (2020). Particle size end meta-analysis of the Qinghai Lake East Sandy and its indicative significance. Quat Res, 40(5): 1203–1215 (in Chinese)

Bokhorst M P, Vandenberghe J, Sümegi P, Łanczont M, Gerasimenko N P, Matviishina Z N, Markovi S B, Frechen M (2011). Atmospheric circulation patterns in central and eastern Europe during the weichse-lian pleniglacial inferred from loess grain-size records. Quat Int, 234(1–2): 62–74

Chai J N, Cha X C, Huang C C, Zhou Y L, Pang R W, Zhang Y Z, Wang N, Cook Y, Rong X Q, Shang R Q (2021). Identification of the genesis of riparian sediments in the Jiaman section of the Yellow River in the Ruoerge Basin. J Lanzhou U (Nat Sci Ed), 57(5): 600–607 (in Chinese)

Chen H T, Kong F B, Xu S J, Miao X D (2021). Dust accumulation processes revealed by loess grain size end metas since the Late Pleistocene in the Miaodao Islands. Quat Res, 41(5): 1306–1316 (in Chinese)

Cheng L Q, Song Y G, Li Y, Zhang Z P (2018). Preliminary application of particle size end-member model in the study of dust sources and paleoclimate of loess in Xinjiang. J Sedimentol, 36(6): 1148–1156 (in Chinese)

Cheng L Q, Yang L H, Long H, Song Y G, Chen Z, Lan M W, Xie M P, Dong Z B (2023a). Early Holocene dust activity variation in the southern Tibetan Plateau and its response to solar irradiance. Palaeogeogr Palaeoclimatol Palaeoecol, 620: 111561

Cheng L Q, Yang L H, Long H, Song Y G, Miao X D, Zhang J R, Wu Y B, Lan M W, Xie M P, Dong Z B (2023b). Milankovitch-paced South Asian monsoons during Marine Isotope Stage 5. Global Planet Change, 225: 104132

Cheng L Q, Yang L H, Long H, Zhang J R, Miao X D, Wu Y B, Lan M W, Song Y G, Dong Z B (2023c). Late Holocene change in South Asian monsoons and their influences on human activities in the southern Tibetan Plateau. Catena, 228: 107153

Dasch E J (1969). Strontium isotopes in weathering profiles, deep-sea sediments, and sedimentary rocks. Geochim Cosmochim Acta, 33(12): 1521–1552

Ding Z L, Derbyshire E, Yang S L, Yu Z W, Xiong S F, Liu T S (2002). Stacked 2.6-Ma grain size record from the Chinese loess based on five sections and correlation with the deep-sea δ^{18}O record. Paleoceanography, 17(3): 5-1−5-21

Ding Z, Lu R, Lyu Z, Liu X (2019). Geochemical characteristics of Holocene aeolian deposits east of Qinghai Lake, China, and their paleoclimatic implications. Sci Total Environ, 692: 917–929

Fang X M, Han Y X, Ma J H, Song L C, Yang S L, Zhang X H (2004). Dust storms and loess accumulation on the Tibetan Plateau: a case study of dust event on 4 March 2003 in Lhasa. Chin Sci Bull, 49(9): 953–960

Gao F Y, Yang J H, Wang S Y, Wang Y J, Li K M, Wang F, Ling Z Y (2021). Variation of the winter mid-latitude Westerlies in the Northern Hemisphere during the Holocene revealed by aeolian deposits in the southern Tibetan Plateau. Quat Res, 107: 104–112

Gou S W, Wu Y Q, Xia D D, Pan J (2012). Spatial and temporal distribution characteristics of winter and spring dust storm frequency and its circulation background on the Qinghai-Tibet Plateau. J Natural Hazards, 21(5): 9 (in Chinese)

Heermance R V, Pullen A, Kapp P, Garzione C N, Bogue S, Ding L, Song P P (2013). Climatic and tectonic controls on sedimentation and erosion during the Pliocene–Quaternary in the Qaidam Basin (China). Geol Soc Am Bull, 125(5–6): 833–856

Jacobs P M, Mason J A, Hanson P R (2011). Mississippi Valley regional source of loess on the southern Green Bay Lobe land surface, Wisconsin. Quat Res, 75(3): 574–583

Kapp P, Pelletier J D, Rohrmann A, Heermance R, Russell J, Ding L (2011). Wind erosion in the Qaidam basin, central Asia:

implications for tectonics, paleoclimate, and the source of the Loess Plateau. GSA Today, 21(4/5): 4–10

Kong F B, Chen H T, Xu S J (2021). Dust accumulation processes and paleoclimatic significance of particle size indication of loess in Zhangqiu, Shandong. J Geog, 76(5): 14 (in Chinese)

Kong X, Zhou W, Beck J W, Xian F, Qiang X, Ao H, Wu Z, An Z (2020). Loess magnetic susceptibility flux: a new proxy of East Asian monsoon precipitation. J Asian Earth Sci, 201(2): 104489

Lai Z P (2006). Testing the use of an OSL Standardised Growth Curve (SGC) for D_e determination on quartz from the Chinese Loess Plateau. Radiat Meas, 41(1): 9–16

Lehmkuhl F, Schulte P, Zhao H, Hülle D, Protze J, Stauch G (2014). Timing and spatial distribution of loess and loess-like sediments in the mountain areas of the northeastern Tibetan Plateau. Catena, 117: 23–33

Li L, Xu C, Zhang Z J, Huang Y D (2021). A review of landslide hazard research on the Loess Plateau. J College Disaster Prevention Sci Techn, 23(4): 11 (in Chinese)

Li S, Yang S L, Liang M H, Cheng T, Chen H, Liu N N (2018). An end-member model study on the particle size distribution of loess on the eastern Qinghai-Tibet Plateau. Earth and Environment, 46(4): 8 (in Chinese)

Li Y, Shi W, Aydin A, Beroya-Eitner M A, Gao G (2020). Loess genesis and worldwide distribution. Earth Sci Rev, 201: 102947

Liang A M, Qu J J, Dong Z B, Su Z Z, Wu B, Zhang Z Y, Qian G Q, Gao J L, Pang Y J, Zhang C X (2020). Particle size end-membership of sediments in the Kumtag Desert and its source insights. China Desert, 40(2): 10 (in Chinese)

Ling Z Y, Yang J H, Wang Z Q, Jin J H, Xia D S, Yang S L, Wang X, Chen F H (2023). Spatiotemporal differences in Holocene climate change in the Yarlung Tsangpo catchment, southern Tibetan Plateau, reconstructed from two sandy loess sequences. Palaeogeogr Palaeoclimatol Palaeoecol, 616: 111473

Liu K, Lai Z P (2012). Chronology of Holocene sediments from the archaeological Salawusu site in the Mu Us desert in China and its palaeoenvironmental implications. J Asian Earth Sci, 45: 247–255

Long H, Wang N, Ma H Z, Li Y (2007). Regional wind and sand characteristics of the lake sedimentary record at the northwest margin of the Tengri Desert. J Sedimentol, 25(4): 626–631 (in Chinese)

Murray A S, Wintle A G (2000). Luminescence dating of quartz using an improved single-aliquot regenerative-dose protocol. Radiation Measure, 32(1): 57–73

Nottebaum V, Stauch G, Hartmann K, Zhang J R, Lehmkuhl F (2015). Unmixed loess grain size populations along the northern Qilian Shan (China): relationships between geomorphologic, sedimentologic and climatic controls. Quat Int, 372: 151–166

Paterson G A, Heslop D (2015). New methods for unmixing sediment grain size data. Geochem Geophys Geosyst, 16(12): 4494–4506

Peck J A, King J W, Colman S M, Kravchinsky V A (1994). A rock-magnetic record from Lake Baikal, Siberia: evidence for Late Quaternary climate change. Earth Planet Sci Lett, 122(1–2): 221–238

Prins M A, Vriend M, Nugteren G, Vandenberghe J, Lu H, Zheng H, Weltje G J (2007). Late Quaternary aeolian dust input variability on the Chinese Loess Plateau: inferences from unmixing of loess grain-size records. Quat Sci Rev, 26(1–2): 230–242

Pye K (1987). Aeolian Dust and Dust Deposits. London: Academic Press

Rea D K, Leinen M, Janecek T R (1985). Geologic approach to the long-term history of atmospheric circulation. Science, 227(4688): 721–725

Roberts H M, Duller G A T (2004). Standardised growth curves for optical dating of sediment using multiple-grain aliquots. Radiat Meas, 38(2): 241–252

Shen C M (2003). Millennial-scale variations and centennial-scale events in the southwest Asian Monsoon: pollen evidence from Tibet. Dissertation for Doctoral Degree. Baton Rouge: Louisiana State University

Song J, Chun X, Bai X M, Sichin B (2016). A review of research on particle size analysis in Chinese deserts. Deserts China, 36(3): 597–603 (in Chinese)

Sun C C, Zhou L M, Zheng X M, Niu R, Meng Q H, Wang L, Du D D, Xu H Y, Wang Z, Chu H M (2016). Peat record of climate change since the Holocene in the Yangbajing Basin, Qinghai-Tibet Plateau. Marine Geol Quat Geol, 36(5): 7 (in Chinese)

Sun D, Bloemendal J, Rea D, An Z S, Vandenberghe J, Lu H Y, Su R X, Liu T S (2004). Bimodal grain-size distribution of Chinese loess, and its palaeoclimatic implications. Catena, 55(3): 325–340

Sun Y, He L, Liang L, An Z (2011). Changing color of Chinese loess: geochemical constraint and paleoclimatic significance. J Asian Earth Sci, 40(6): 1131–1138

Sun Z X , Jiang Y Y , Wang Q B ,Owens P R (2018). A fractal evaluation of particle size distributions in an eolian loess-paleosol sequence and the linkage with pedogenesis. Catena, 165: 80–91

Sweeney M R, Mason J A (2013). Mechanisms of dust emission from Pleistocene loess deposits, Nebraska, USA. J Geophys Res Earth Surf, 118(3): 1460–1471

Thompson L G, Yao T, Mosley-Thompson E, Davis M E, Henderson K A, Lin P N (2000). A high-resolution millennial record of the South Asian Monsoon from Himalayan ice cores. Science, 289(5486): 1916–1919

Újvári, Kok J F, Varga G, Kovács J (2016). The physics of wind-blown loess: implications for grain size proxy interpretations in Quaternary paleoclimate studies. Earth Sci Rev, 154: 247–278

van Hateren J A, Prins M A, van Balen R T (2018). On the genetically meaningful decomposition of grain-size distributions: a comparison of different end-member modelling algorithms. Sediment Geol, 375: 49–71

Vandenberghe J (2013). Grain size of fine-grained windblown sediment: a powerful proxy for process identification. Earth Sci Rev, 121: 18–30

Wang J M, Pan B T (1997). Basic characteristics of loess deposition and its environment in the eastern Qinghai-Tibet Plateau. Desert China, 17(4): 395–402 (in Chinese)

Wang N L, Yao T D, Thompson L G, Henderson K A (2002). Evidence from the Guria ice core record of an early Holocene intense cooling event. Sci Bull (Beijing), 47(11): 6 (in Chinese)

Wang Q S, Song Y G, Li J J, Zhao Z J, Rong P (2015). Color characteristics and paleoclimatic significance of late glacial-

interglacial cyclonic Chaona loess. Geoscience, 35(11): 1489–1494 (in Chinese)

Wang Z D, Huang C C, Yang H J, Zha X C, Zhou Y L (2018). Physical source characteristics and evolution of loess grain size indication since the Late Pleistocene in the eastern foothills of Liupan Mountain. Geoscience, 38(5): 818–826 (in Chinese)

Wang Z J, Chen S T, Zhou X Q, Liang Y J, Wang Y J (2020). Spectral characteristics of millennial scale events of Asian monsoon during the last Glacial Period. Quat Res, 40(4): 13 (in Chinese)

Weltje G J (1997). End-member modeling of compositional data: numerical-statistical algorithms for solving the explicit mixing problem. Math Geol, 29(4): 503–549

Xiong J L, Fan X M, Dou X Y, Yang Y H (2021). Seasonal variation of Yalong glacier flow velocity in the Ranwu Lake basin, southeast Tibet. J Wuhan U (Inform Sci Ed), 46(10): 1579–1588 (in Chinese)

Xu L Y, Yang L H, Zhang S, Zhai T C (2021). Particle size end meta-analysis and indicative significance of reticulated laterite in Xuancheng Xiangyang profile. Earth Environ, 49(6): 646–654 (in Chinese)

Xu X W, Qiang X K, An Z S, Li X B, Li P, Sun Y F (2010). Magnetic susceptibility records of lacustrine core in Heqing Basin and its paleoenvironmental significance. Chinese J Geomech, 16(4): 372–382 (in Chinese)

Yang F, Zhang G L, Yang F, Yang R M (2016). Pedogenetic interpretations of particle-size distribution curves for an alpine environment. Geoderma, 282: 9–15

Yang J H, Xia D S, Gao F Y, Wang S Y, Li D X, Fan Y J, Chen Z X, Tian W D, Liu X Y, Sun X Y, Wang Z Q, Wang F (2021). Holocene moisture evolution and its response to atmospheric circulation recorded by aeolian deposits in the southern Tibetan Plateau. Quat Sci Rev, 270: 107169

Yang L J, Ma X C, Jia J J, Yan J, Luan Z D (2020). Effects of Yellow River diversion and sand transport changes on the particle size characteristics of muddy wedge sediments in Shandong Peninsula over the past 100 years. J Oceanogr, 42(1): 78–89 (in Chinese)

Yang S L, Chen Z X, Chen H, Luo Y L, Liu L, Liu X J, Li Q, Zhou J T, Li P U (2022). Magnetic properties of the Ganzi Loess and their implications for precipitation history in the Eastern Tibetan Plateau since the Last Interglacial. Paleoceanogr Paleoclimatol, 37(2): e2021PA004322

Yang S L, Ding Z (2014). A 249 kyr stack of eight loess grain size records from northern China documenting millennial-scale climate variability. Geochem Geophys Geosyst, 15(3): 798–814

Yang S, Ding Z L (2003). Color reflectance of Chinese loess and its implications for climate gradient changes during the last two glacial-interglacial cycles- art. no. 2058. Geophys Res Lett, 30(20): 2003GL018346

Zan J B, Fang X M, Yang S L, Yan M D (2013). Evolution of the arid climate in high Asia since 1 Ma: evidence from loess deposits on the surface and rims of the Tibetan Plateau. Quat Intern, 313–314: 210–217

Zan J B, Li X J, Kang J, Guo Z G, Mao Z Q (2020). Intensified pedogenesis caused the increase in the fine particle content of late Cenozoic fluvial and lacustrine deposits in the NE Tibetan Plateau. Sediment Geol, 398: 105587

Zhang, J F, Feng J L, Hua G, Wang J B, Yang Y B, Lin Y C, Jiang T, Zhu L P (2015). Holocene proglacial loess in the Ranwu valley, southeastern Tibet, and its paleoclimatic implications. Quat Intern, 372: 9–22

Zhao C, Liang J T, Wang J C, Yang L, Zhang S (2019). Remote sensing analysis of glacier dynamics changes in the Palungzangbu basin (Bomi-Ranwu profile). Sci Techn Eng, 19(21): 7 (in Chinese)

Zhong N, Jiang H C, Li H B, Xu H Y, Liang L J, Shi W (2020). Particle size end-member inversion of lacustrine sediments from Xinmacun in the upper Minjiang River and its recorded tectonic and climatic events. J Geol, 94(3): 968–981 (in Chinese)